PHYSICAL INVESTIGATION OF A CAVITATION VORTEX COLLAPSE

Ph. Couty, M. Farhat, and F. Avellan
Laboratory for Hydraulic Machines
EPFL-Swiss Federal Institute of Technology of Lausanne
Switzerland

Abstract

Most of severe cavitation erosion of hydraulic machines are found to be associated with the collapse of transient cavitation vortices downstream of a leading edge cavity. The dynamics of such a type of cavitation is studied in a Cavitation Vortex Generator (CVG). By producing the cyclic growth and collapse of a single cavitation vortex, this device provides a way to investigate the mechanisms involved in the final stage of the vapour cavity collapse.

The observations of vapour structures and emitted shock waves are based on high-speed visualisations (up to 210^6 frames/s) which are obtained by using a shadowgraph video system. Luminescence sources which are emitted during the collapse are visualised by using an intensified camera. By adjusting a short exposure time of 500 ns before shock waves are captured, this allows the time of minimum cavity volume and position to be estimated. This paper presents the complex physical mechanisms of cavitation vortex collapse which have been pointed out with these simultaneous visualisations.

1 Introduction

Physical mechanisms involved in cavitation phenomenon are still not fully understood. Nevertheless, it is nowadays assumed that repetitive collapse of vapour cavities in liquid can yield a severe erosion if this occurs near a solid surface. This erosion is observed on blades of hydraulic machines or blade profiles (Pereira, 1998), where a limited accessibility doesn't allow local vapour cavity collapses to be visualised. Thus, the need of investigations on the dynamics isolated vapour cavities, pushes to study near wall collapsing bubble (Tomita et al., 1986)(Lauterborn)(Vogel et al., 1989) or vortices (Avellan et al., 1989). High-speed visualisations have allowed physical mechanisms involved in cavitation erosion to be apprehended. They can be either shock wave impact or micro-jet, which come with the last stage of cavity collapse. These phenomena act as intense pinpoint loads as high as 1GPa (Farhat, 1994) on the material and they are therefore directly involved in the erosion process. The intensity of such pressure impacts due to supersonic rebounds of bubble collapse has also been numerically first estimated by Hickling and Plesset (1964). In order to study the collapse of vortices, such as they can be observed in many real cavitating flow, a special vortex cavitation generator (CVG) can be used. By producing a cyclic growth and collapse of a single cavitation vortex , we can study the cavity dynamics in the test section of the CVG.

The aim of this paper is to describe the physical characteristics of the final stage of the cavitation vortex collapse: vapour structure pattern, shock waves and the luminescence phenomenon coming with the collapse.

First, the hydraulic operation of CVG is briefly described. Second, the instrumentation is presented. This involves a high-speed shadowgraph video system as well as the implementation of a light intensified CCD camera. Third, it is explained how the image processing of the high-speed visualisations and of luminescence visualisation patterns, is carried out in order to study shock wave emission and the vapour phase evolution. Finally, simultaneous visualisation results of luminescence and shock waves will be presented.

2 The Cavitation Vortex Generator

2.1 Principle of operation

The cavitation vortex generator CVG whose components are given figure 1, is a closed loop consisting of a test section, where the erosion tests and visualisations are performed, a rotating valve, a number of pressure vessels and a circulating pump. The pump draws water from an atmospheric pressure vessel through a heat exchanger. This last vessel plays the role of dumping chamber to reduce the pressure pulsations in the circuit. The maximum flow rate is 2.7 $m^3 \cdot s^{-1}$ for an upstream pressure of 0.84 MPa. The test section is made up of a cylindrical chamber, which is ended on one side with a prismatic section and on the other side with a pipe that leads to downstream vessels. A tangential inlet in the test section creates a vortex flow.

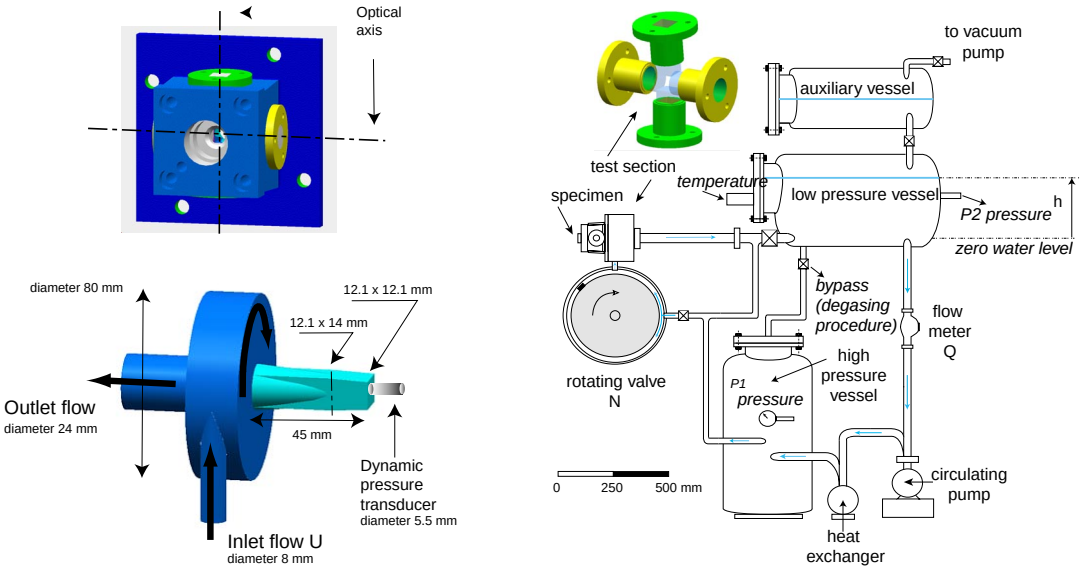

Figure 1: The Cavitation Vortex Generator of IMHEF

The principle of CVG is to produce a serie of low-pressure and high-pressure waves in the vortex flow. A phase change occurs in a part of the vortex, followed by a violent collapse, at each revolution of the valve. While the valve is open, a rotation is initialised in the test section and the downstream pipe. As the valve closes a water hammer is created in the loop : a low pressure wave then propagates in the test section and its downstream pipe. Due to this, a vapour core is created on the vortex axis, tending to extend to the entire radius of the pipe. The closure duration of the valve which depends on the rotational velocity, limits the expansion of the vapour core. When the valve reopens, the pressure wave coming from the upstream vessel causes the vapour cavity to collapse.

2.2 Hydrodynamic parameters

The hydrodynamic parameters of CVG are the flow rate Q, the cavitation number σ and the speed of rotation of the rotating valve N. Pressures are measured with 2 piezoelectric pressure transducers (*Keller*Ⓡ) in both high pressure vessel (p_1, 0-10 bar range), and low pressure vessel (p_2, 0-1 bar range). The hydrodynamic parameters Q and σ can be expressed as a function of pressures p_1 and p_2 by introducing a head loss coefficient of the circuit :

$$Q = K\sqrt{(p_1 - p_2)} \text{ with } K = 0.26\, kg^{-\frac{1}{2}}.m^{-\frac{3}{2}} \tag{1}$$

$$\sigma = \frac{p_2 - p_v(T)}{\frac{1}{2}\rho U^2} \tag{2}$$

In order to maintain the amount of dissolved gas in water below an acceptable value, a degassing procedure is realised before each experiments. By this way, the measured O_2 contents is less than 2 ppm for a time duration of experiments smaller than 2 hours. The temperature has been controlled and regulated between $14°C$ and $15°C$ for all conditions.

2.3 Test section

A global view of the entire test section (bulk flow) is given figure 1. The end of test section is a prismatic chamber resulting from the intersection of 2 rectangular prism glasses and 2 cylindrical glasses. These are mounted in metal sleeves, which are fixed to a monoblock structure. The test section has two parallel faces formed by cylinders, and 2 faces with an angle of 3.72° formed by rectangular prisms. Thus, simultaneous visualisations with perpendicular axes can be achieved. In order to measure pressure transients during the collapse, the usual material sample mounted on end test section is replaced by a piezoelectric pressure transducer. This is *Kistler*® type (200 bar range, 130 kHz natural frequency, 1 μs rise time). Due to the short time constants involved, pressure transducer is exploited in its natural frequency bandwidth. Consequently, values of pressure peak must be considered with care.

3 Visualisation systems

3.1 Low level light detection

An intensified light video camera is used for the visualisations of luminescence sources. This camera is a *QUICK 05A* ® model. The main characteristic of this camera is to be constituted of a Phosphor Micro Channel Plate (MCP) for the light intensification stage which is coupled with a video CCD image sensor via high quality optic. The shutter can be triggered by a TTL signal for acquisition on events directly on the camera, and the time delay for effective triggering is 30 ns. The image resolution is 572 × 290 pixels, and the object resolution is 30 μm × 60 μm. The frames are grabbed on a PC.

3.2 High-speed shadowgraph

In order to visualise the high pressure gradient produced during the very last moments of vortex collapse, a shadowgraph technique has been used. Since the complete collapse process that must be observed has a very short time duration, down to 1 μs, a high-speed Cranz-Schardin shadowgraph system is used.

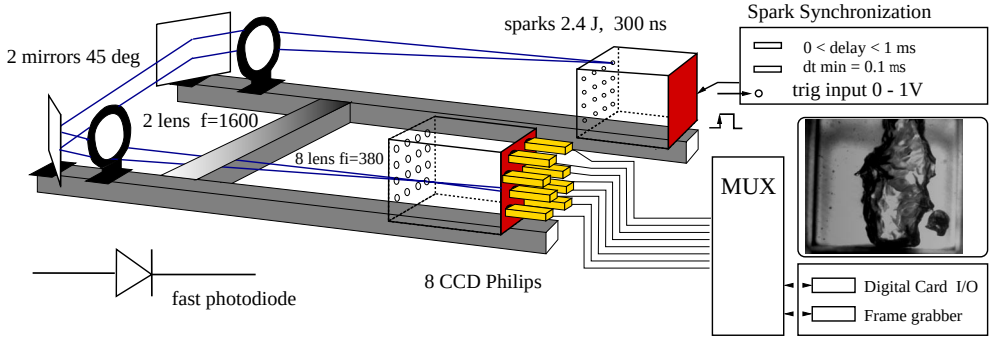

Figure 2: The Cranz-Schardin video shadowgraph camera

The principle of this system is still very close to the original Cranz-Schardin camera. Substantial efforts have been made to replace the photosensitive film by a set of CCD image sensors. This new camera takes advantaged both of the versatility of digital images for processing and the simplicity of the Cranz-Schardin camera (Couty, 1999). This system is presented figure 2. Short duration light sources are provided by a set of spark generator which have a mean time exposure of 300 ns. Discharges are controlled by an electronic

time unit, which provides an adjustable spark rate of 1 kHz to 10 MHz. As the maximum jitter is 200 ns, a photodiode is used to detect exact occurrences of flashes.

The video system is composed by a PC equipped with a Matrox Genesis frame grabber, a digital I/O data card for synchronisation purposes, 8 CCD image sensors and a video control unit. Acquisition can be armed on an asynchronous event. After flashes emission and integration period of 17 ms of image sensors is achieved, frames are then transferred in the storage section of the image sensor and can be further sequentially retrieved by the frame grabber through the video control unit (MUX). The final image resolution is 754 $\times$ 288 pixels and the resolution of object is 30 $\mu m \times$ 60 μm.

3.3 Synchronisation of visualisations

As the collapse time can not be predicted better than of the order of millisecond if the reference time is based on the closure of valve, both sparks of the high-speed shadowgraph and the electric gate of the intensified camera are triggered on a threshold of the dynamic pressure signal through an oscilloscope. This is armed on the valve closure trigger as well as the video system. By this way, the asynchronous integration period of all image sensors are started before sparks emit light. The detailed synoptic of the acquisition is presented figure 3.

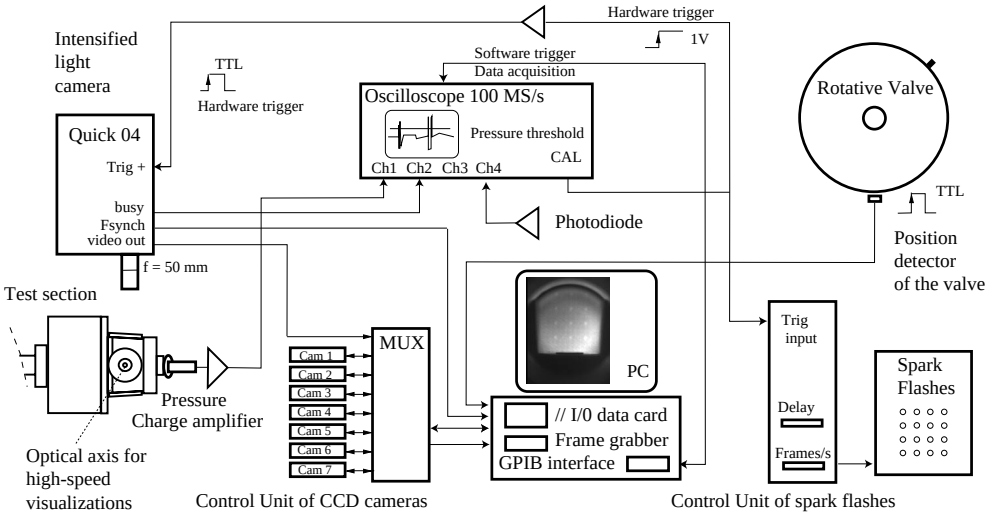

Figure 3: Synoptic of the simultaneous visualisations

4 Results

4.1 Luminescence of the vortex

A preliminary study of the luminescence of the vortex have been realised before going on simultaneous visualisations of shock waves and luminescence. The aim of these experiments is to characterise the luminescence in term of time occurrence, space, and intensity for various hydrodynamic conditions. In order to point out the different characteristics of luminescence, an adapted image processing has been implemented. A global representation of statistical localisation of luminescence emission is obtained by superposing images data through a suitable threshold operation. In order to study into details each luminescence image data, labelling of connected luminescence spots can be performed. Spatial "mass" centre of each binary entity (luminescence spots) is then calculated by taking the corresponding original pixel values as virtual weight masses. The sum of pixel values for each luminescence entity is attributed to each centres and is defined as the luminescence intensity of the luminescence entity.

Obtained superposed image data for the condition Q = 0.58 l/s and the time window of interest $[0, 10\mu s]$ from pressure trigger are represented figure 4, where test section border is drawn in white. In order to maximise the number of photons, the gain of camera has been set to maximum. The corresponding success rate of luminescence detection is 400 over a total of 714 detection attempts. Others time windows have been investigated, the obtained luminescence spots are spread over the entire test section, with success rates less than 5%.

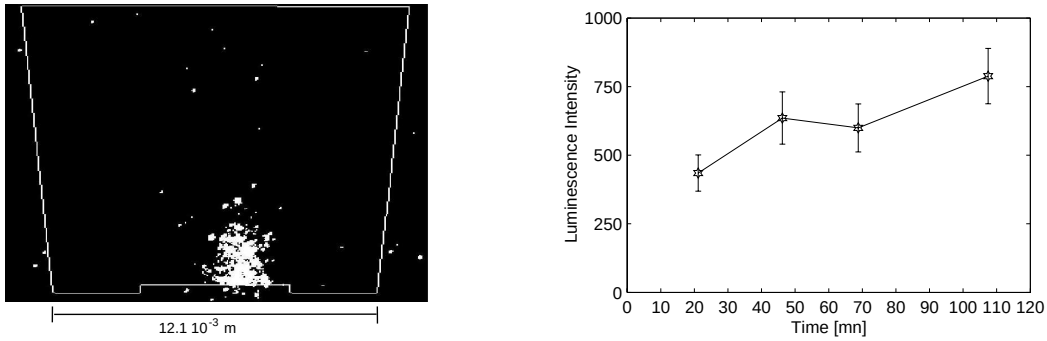

Figure 4: Superposition of 400 luminescence emission sources at time window $[0\mu s, 10\mu s]$ and time evolution of luminescence intensity, Q=0.58 l/s, σ=1.57, N=200 rpm

The corresponding luminescence spot centres and intensity can be calculated. The mean distance to the wall of collapses is $0.4\,10^{-3}m$, and mean deviation distance from test section axis is $0.7\,10^{-3}m$. The luminescence intensity is not correlated with the maximum value of pressure which is actually principally weighted by the distance of the collapse from its centre (not represented). Average values of luminescence intensity for 4 series of 100 acquisitions, as well as standard deviation are given figure 4 (error bars on graphic must be multiplied by 10). The global increase of luminescence with time can be explained by the increasing dissolved gas in water.

4.2 The last stage of vortex collapse

4.2.1 Image processing of high-speed visualisations

In order to trace shock wave front propagation and vapour wall evolution, an image processing procedure has been developed. First of all, each image of sequences are aligned and calibrated by placing a grid target in test section. Then, image intensity is scaled and threshold in order to isolate vapour cavity contour in a definite region of interest. By this way, the main geometric characteristics of vapour cores are calculated : centre, area and equivalent radius.

At last, the displacement of shock wave front is calculated by using an intercorrelation method. In order to do this, a polar to rectangular transform is operated by taking the origin of the transformation as the calculated centre of the main vapour cavity and by defining a sector of interest. Indeed, the shock front appears to be straight and horizontal instead of being circular. Afterwards, a normalised intercorrelation between consecutive warped images gives the vertical displacement of shock wave front which is equivalent to the difference in radius. The result is validated by superposing the original sequences with obtained contours.

4.2.2 Shock waves

The present study has been restricted to 2 hydrodynamic conditions :
- N = 200 rpm, Q = $0.76\,10^{-3}m^3/s$ and $\sigma = 0.91$
- N = 200 rpm, Q = $0.58\,10^{-3}m^3/s$ and $\sigma = 1.57$

For both hydrodynamic conditions, a systematic strong shock waves emission comes with the main cavity collapse. Most of collapse centres are situated near the wall as it was already demonstrated by luminescence results. In order to visualise vapour phase before the emission of shock wave, the pressure threshold has been

set to a minimum which is approximately equal to 0.4 MPa. The maximum value of the pressure signal is quite delayed with the departure of shock wave, and the pressure transducer is actually excited to its natural frequency of 130 kHz. Example of pressure signal with the corresponding image sequence is given figure 5.

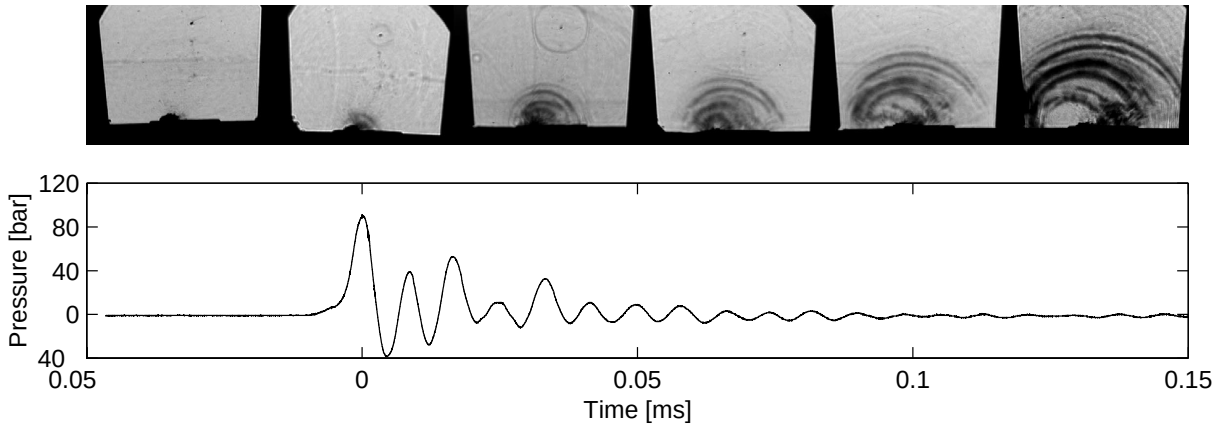

Figure 5: Pressure signal and emission of multiple shock waves, 10^6 fps, N=200 rpm, Q=0.76 l/s, σ=0.96

Based on image analysis of visualisations, the physical characteristics of shock waves can be established. First, the "epicentre" of the wave corresponds to the centre of the vapour phase. Second, before the shock front is clearly detached from the vapour cavity and propagates spherically at nearly sound speed with mean value of 1380 m/s and standard deviation 50 m/s (40 samples), the vapour cavity is initially surrounded by a dark contrast which can be explained by a high change in the refractive index due to the shock formation. This dark zone merges with the shadow of the vapour phase. Therefore, it is not evident to distinguish the volume of the vapour phase from this pattern. Therefore, because both lack of contrast and lack of time resolution, it is not possible to argue on the time of departure of the shock and the time of minimum radius. Third, the incident wave propagates in water until it reflects on sides of test section. In case of near wall collapse, the incident wave is immediately followed by a reflected wave which propagates in the same direction than incident shock wave with the same celerity. Finally, instead of an incident shock wave with an unique and definite wave front, wave pattern is more like a radiated multiple shock waves. This feature is particularly illustrated by sequence figure 5, where wave fronts are numerous and where epicentre of shock waves are not unique. With the same idea, it is worth noting that the observed thick waves are not due to blur effects. This has to be related with the nature of the pressure transient. This argument have been stated by comparing on same pictures the thickness of two different waves having the same propagation celerity.

4.2.3 Vapour cavity

The vapour cavity shape and arrangement are extremely variable. As it has been mentioned in the preceeding paragraphs, vapour cavities are preferentially collapsing near the surface transducer. However, as observation near the transducer surface is partly occulted because of parallax effects, this study has been focused on far wall cavity collapse.

The vapour cavities are rarely spherical and isolated, a main cavity is usually coming with others secondary smaller cavities. These cavities can be the epicentres of different emitted shock waves which can be delayed in time. Moreover, even for a single cavity, it appears that this does not collapse in a regular way. Consequently, a cavity may cause the departure of delayed shock waves at different epicentres. Different pattern of obtained cavities are given in sequences of figure 7. Concerning the vapour growth at rebound, average value of velocities of 180 $m \cdot s^{-1}$ with maximum values of 300 $m \cdot s^{-1}$ have been estimated for both hydrodynamic conditions. The growth rate is then rapidly diminishing in a same way that it is depicted figure 6.

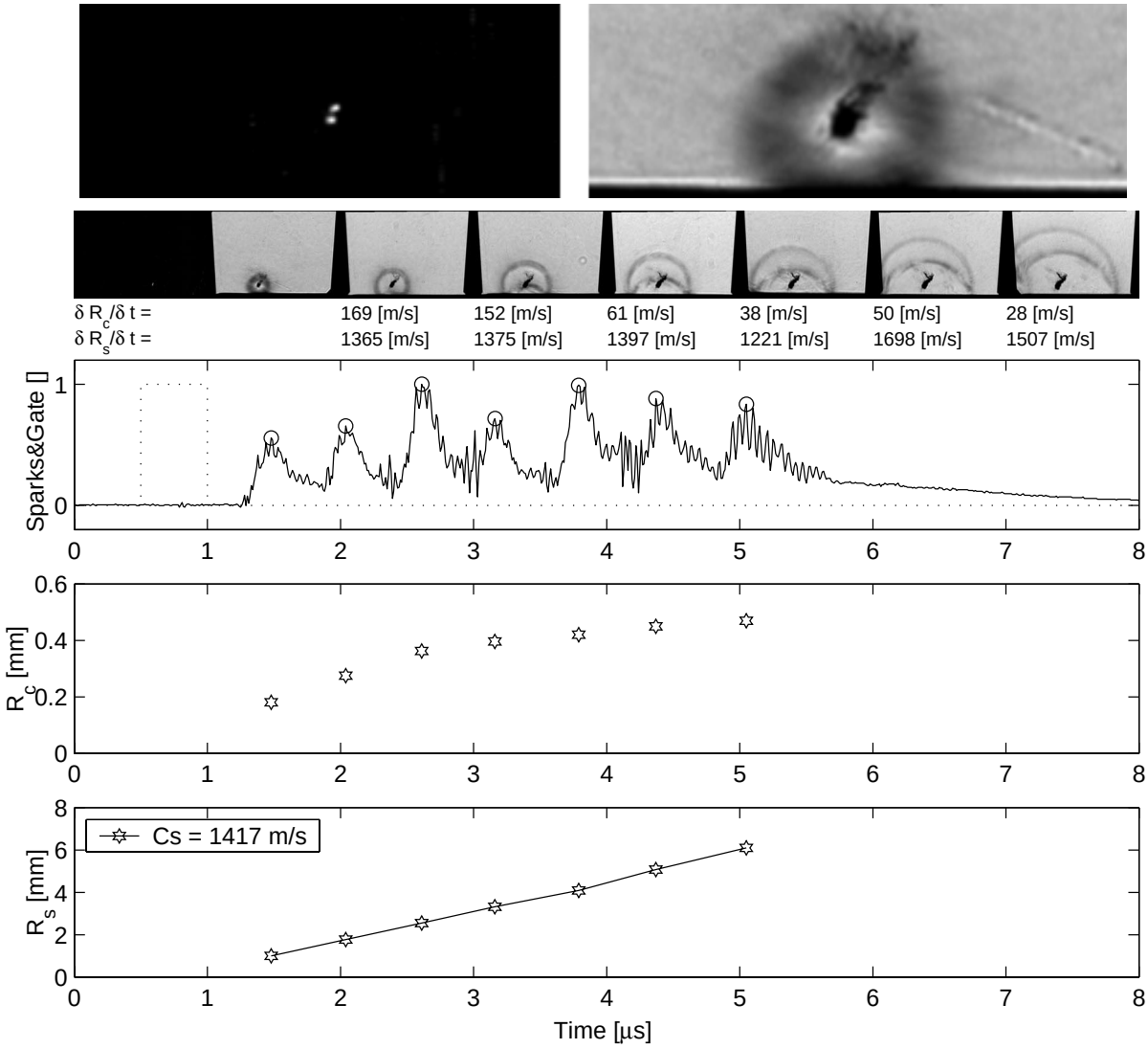

Figure 6: Simultaneous captures of luminescence and shock wave, 210^6fps, N=200rpm, Q=$0.58l/s$, σ=1.57

4.2.4 Simultaneous visualisations

Assuming luminescence is emitted if vapour volume reached its minimum volume (Barber and Putterman, 1992), simultaneous visualisations could provide a way to estimate shock wave front celerity at departure by considering the first image of high-speed visualisations that is following the luminescence emission. For this purpose, the exposure time of intensified camera has been adjusted to 500 ns and 210^6 fps for high-speed visualisations. An example of the simultaneous visualisation is given figure 6 where values of wave radius R_s, equivalent vapour radius R_c, as well as vapour growth velocities $\frac{\delta R_c}{\delta t}$ and wave celerities $\frac{\delta R_s}{\delta t}$ at different times are given. The emission of a double luminescence source is clearly visible on top left of the figure. However, luminescence are principally unique. According to width of time exposure and time of captured images, the estimated celerity of shock wave at departure lies between 1000 and 2000 $m \cdot s^{-1}$. Anyway, this result demonstrates that supersonic celerities must concern the very vicinity of vapour phase at collapse time. This fact is actually is in good agreement with recent results obtained for sonoluminescing bubble (Holzfuss, 1998).

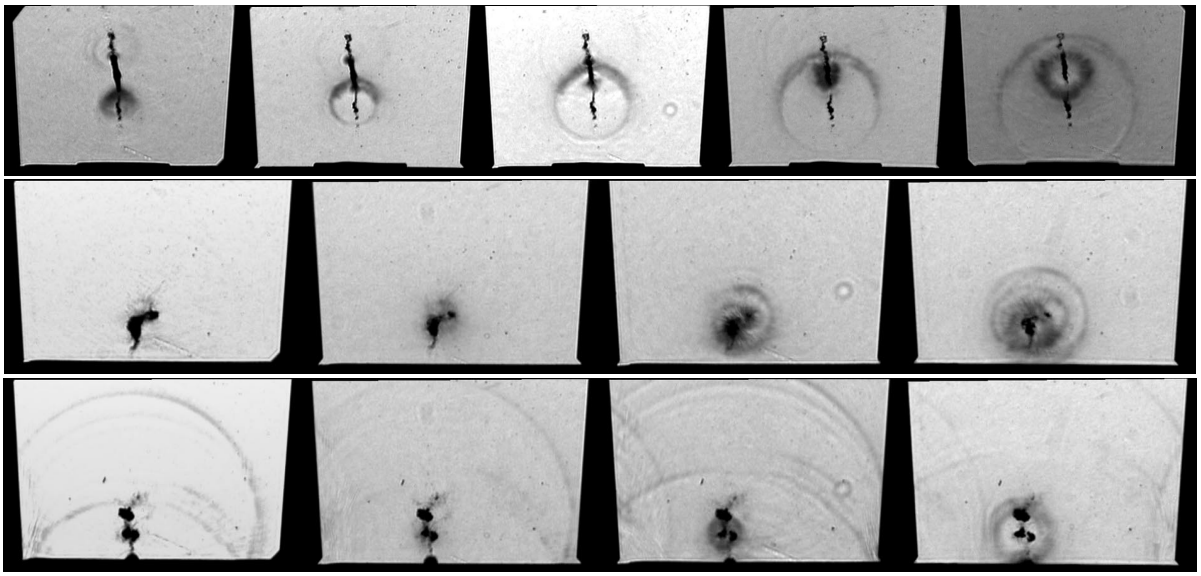

Figure 7: 3 examples of various vapour phase history, 210^6 fps, N=200 rpm, Q=0.76 l/s, σ=0.96

5 Conclusions

This paper has confirmed the complex physical characteristics involved in the collapse of a cavitation vortex. Firstly, the vortex collapse leads to an irregular and unpredictable vapour cavity shape at the final stage. Secondly, estimations of interface velocity result in maximum values of 300 $m \cdot s^{-1}$ at rebound. These cavities can fission and emit various pressure transient from different epicentres, and principally multiple and delayed shock waves. These shock waves can be either clearly segregated or superposed which leads to an apparent thick front of pressure transient which propagates at nearly sound speed. Finally, the simultaneous visualisations has demonstrated that luminescence sources mingle with the shock wave epicentres. Furthermore, we have shown that luminescence and shock wave ignition occur within a time interval less than 1 μs.

References

Avellan, F., Farhat, M., (1989) Shock Pressure Generated by Cavitation Vortex Collapse, *Int. Symp. on Cavitation* **88**, 119-125

Barber, B. P. and Putterman ,S. J., (1992) Light scattering measurements of a repetitive supersonic implosion of sonoluminescing bubble *Phys. rev. Lett.* **69**, 3839

Couty, Ph., Farhat, M., Avellan, F., (1999) Visualisation du collapse de cavites et Sonoluminescence, *FLUVISU99*, France

Farhat, M., (1994) Contribution a l'étude de l'érosion de cavitation: mécanismes hydrodynamiques et prédiction Ph.D. Thesis **1273** E.P.F.L, Switzerland

Hickling, R., Plesset, M., (1964) Collapse and Rebound of Spherical bubble in water *Phys. of Fluid* 7, 1

Holzfuss, J., Ruggeberg, M., Billo A. (1998) Shock Wave Emissions of a sonoluminecing Bubble *Phys. rev. Lett.* **81**, 23

Vogel, A., Lauterborn, W., Timm, R., (1989) Optical and acoustic investigations of the dynamics of laser-produced bubbles near a solid boundary *J. Fluid. Mech.*, **206**, 299-338

Pereira, F., Avellan, F., Dupont, Ph., (1998) A Statistical Approach to the study of Transient Erosive Cavities on a 2D profile *J. Fluid. Eng.*, **226**, 71-79

Tomita, Y., Shima., A., (1986) Mechanisms of impulsive pressure generation and damage pit formation by bubble collapse *J. Fluid Mech.*, **169**, 535-564